

## Ta-10W 难熔合金光纤激光焊接工艺研究

杜欣, 祁百鑫, 赵振家, 张桐, 武强\*, 邹江林, 肖荣诗

北京工业大学材料与制造学部高功率及超快激光先进制造实验室, 北京 100124

**摘要** 采用 6 kW 多模光纤激光器进行了 Ta-10W 难熔合金的光纤激光焊接工艺研究。利用高速摄像机、光学显微镜、扫描电镜、显微硬度仪及拉伸试验机对焊缝成形、熔池形态、飞溅物形态、显微组织、显微硬度、接头强度及断口形貌进行分析。研究表明,在焦点位于板材表面且焦点直径为 0.3 mm 的聚焦参数下,当焊接速度为 2~3 m/min,激光功率为 1.5~2.0 kW 时,焊接模式由热导焊转变为深熔焊。Ta-10W 深熔焊时焊缝成形良好,焊接飞溅大且飞溅物不易附着于板材,焊缝呈钉头形。3 mm 厚对接接头的焊缝组织主要为柱状晶,在焊缝靠上的位置,主要为垂直于板厚方向的细长晶粒;在焊缝中部与下部,形成的则是细等轴晶粒。拉伸试验结果显示,接头的室温拉伸强度为 506.5 MPa,约为母材的 92.1%;1500 °C 高温拉伸强度约为 140.9 MPa,接头断裂在母材处。

**关键词** 激光技术; Ta-10W; 难熔合金; 激光焊接; 微观组织; 力学性能

中图分类号 TG442

文献标志码 A

DOI: 10.3788/CJL202249.1602006

## 1 引言

钽(Ta)和钨(W)等难熔金属及其合金具有较大的密度、较高的熔点、良好的加工性能和抗熔融金属腐蚀等优异的物化性质<sup>[1]</sup>,被广泛应用于电子工业、武器制造、航空航天和核工业等领域<sup>[2]</sup>,在国民经济与国防科技中占有重要地位。其中,钽(Ta)和钨(W)的晶体结构均为体心立方(BCC)结构,可以形成二元连续固溶体合金<sup>[3]</sup>。这种难熔合金是以钽为溶剂,钨为溶质,一般通过真空电子束熔炼或者是粉末冶金等方法制成<sup>[4-5]</sup>。另外,Ta-10W 合金除难熔合金的上述优点外,还具有高温强度高、抗热震性能好、线胀系数小等优点,特别适用于制备航天领域服役于极高热条件下的关键构件<sup>[6]</sup>。

目前,钽钨合金的焊接常采用氩弧焊、真空扩散焊和真空电子束焊等方法完成。丁旭<sup>[7]</sup>通过氩弧焊实现了 Ta-12W 合金的连接。由于热输入较高,焊缝晶粒较大,热影响区晶粒严重粗化;拉伸试验表明,试样断裂在热影响区,强度为 438 MPa。Tao 等<sup>[8]</sup>采用真空电子束工艺实现了 Ta-10W 与 GH3128 的焊接,并进行了焊后固溶处理;研究表明,固溶处理可有效消除接头微裂纹,并使元素发生充分扩散,焊缝组织由树枝晶变为块状奥氏体,并析出大量的合金碳化物。Chen 等<sup>[9]</sup>研究了纯钽与纯钨的电子束焊接,发现焊缝成形不良,接头内部存在大量的裂纹与缩孔,强度仅为

56 MPa;采用将电子束作用位置偏向 Ta 母材的方法进行焊接,得到了成形与组织良好的焊缝。此外,该团队研究了 TC4 与 Ta-12W 异种材料的电子束对接焊接工艺,发现电子束偏向 TC4 母材 0.4 mm 时,接头强度与钽钨合金母材强度基本相等,焊缝中存在游离态单质钽<sup>[10]</sup>。Luo 等<sup>[11]</sup>采用 Ni 箔作为中间层,通过真空扩散焊,实现了 93W 与 Ta 的连接,接头强度为 202 MPa,接头断裂在 Ni-Ta 界面,断裂模式为韧性断裂,在断裂界面上形成了大量的 Ni<sub>4</sub>W、Ni<sub>2</sub>Ta 和 Ni<sub>3</sub>Ta 等金属间化合物。

与 CO<sub>2</sub> 激光相比,光纤激光具有材料吸收率高、加工柔性大、运行稳定性高等突出优点<sup>[12-13]</sup>,被广泛用于铝合金、高温合金及陶瓷材料等高反、高热强度及高熔点材料的加工<sup>[14-17]</sup>。但由于其通常在大气环境中实施,光纤激光焊接存在熔池波动大、羽辉喷发速度高、焊接飞溅大等特点<sup>[18-19]</sup>。另外,Ta-10W 的气体相容性较差且对杂质元素极其敏感,该合金在 300 °C 时开始吸氧,340 °C 时吸氢,700 °C 吸氮,严重影响其力学性能与高温加工性能<sup>[1]</sup>。对 Ta-10W 光纤激光焊接工艺提出了严峻的挑战。

本文通过对 Ta-10W 合金板材进行光纤激光扫描焊与对接焊,研究了焊接功率及焊接速度对焊缝形貌的影响规律,获取了热导焊转变为深熔焊接时的功率阈值。另外,对 Ta-10W 对接接头的焊缝形貌及微观组织进行了观测,并对接头进行了显微硬

收稿日期: 2021-11-01; 修回日期: 2021-11-15; 录用日期: 2021-11-22

基金项目: 国家自然科学基金面上项目(51775009)

通信作者: \*jlwuqiang@bjut.edu.cn

度及拉伸力学性能测试,分析了断口形貌及断裂特征。

## 2 试验方法及设备

试验材料为真空电子束熔炼的 Ta-10W 难熔合金板材,其组织主要为单相钽钨固溶体。材料的物性参数如表 1 所示。试验设备为 YLS-6000 多模光纤激光器,光束波长为 1060~1070 nm,光束聚焦参数  $K_f = 8 \text{ mm} \cdot \text{mrad}$ ,传输光纤芯径为 200  $\mu\text{m}$ ,输出耦合准

直镜的焦距为 200 mm,聚焦镜的焦距为 300 mm,聚焦光斑直径为 0.3 mm。采用五轴三维加工平台实现运动轨迹及焊接工艺参数的控制。试验装置示意图如图 1 所示,采用气体保护喷嘴对深熔小孔和熔池进行保护;同时,在焊缝背部实施背保护。保护气采用高纯氩气(体积分数为 99.999%),保护喷嘴熔池流量为 8 L/min,背部流量为 8 L/min。在焊接时采用高速摄像机和半导体照明激光观察熔池形貌与焊接飞溅。

表 1 Ta-10W 的物性参数

Table 1 Physical property parameters of Ta-10W

| Parameter | Density $\rho / (\text{g} \cdot \text{cm}^{-3})$ | Melting point $T_m / ^\circ\text{C}$ | Strength $\sigma_b / \text{MPa}$ | Ductility $\delta / \%$ | Hardness /HV | Liner expansivity $\alpha / \text{K}^{-1}$ |
|-----------|--|--------------------------------------|----------------------------------|-------------------------|--------------|--|
| Value     | 16.8   | 3035                                 | 550                              | 25                      | 288          | $6.7 \times 10^{-6}$                       |

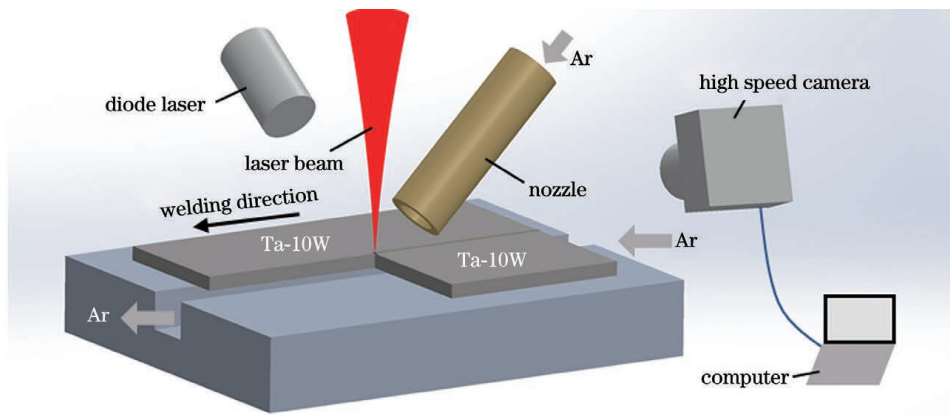


图 1 试验装置示意图

Fig. 1 Schematic of test device

试验前用砂纸对板材表面进行打磨、抛光,并用丙酮清洗。试验主要分为两部分。第一部分是平板扫描试验,采用尺寸为 50 mm×20 mm×4 mm 的 Ta-10W 板材,在光束离焦量  $f = 0 \text{ mm}$  与上述保护气流量下进行扫描焊接试验,焊接参数如表 2 所示。其中,  $v$  为焊接速度,  $P$  为激光功率,采用正交试验的方式,进行参数组合。焊后制备金相试样,试样腐蚀液为氢氟酸和硝酸的混合液(HF 与  $\text{HNO}_3$  的体积比为 1:1),采用 VK-X130K 超景深显微镜观察焊缝形貌,并测量各焊接参数下焊缝的熔深与熔宽。

表 2 焊接参数

Table 2 Welding parameters

| Parameter                              | Value                                  |
|--|--|
| $v / (\text{m} \cdot \text{min}^{-1})$ | 2.0, 3.0, 4.0                          |
| $P / \text{kW}$                        | 1.5, 2.0, 2.5, 3.0, 3.5, 4.0, 4.5, 5.0 |

第二部分是对接焊试验,采用厚度为 3 mm 的 Ta-10W 板材,焊接参数为:激光功率  $P = 4 \text{ kW}$ ,焊接速度  $v = 3 \text{ m/min}$ ,离焦量  $f = 0 \text{ mm}$ ,保护气参数如前所述。焊后制备金相试样,采用超景深显微镜和 FM-300e 型显微硬度计进行焊缝形貌和微观组织分析及显微硬度测试。分别制备室温和高温拉伸试样,在

CMT5305 拉伸试验机和高温力学试验机上进行接头的室温和高温力学性能测试。依据测试设备要求,室温与高温拉伸试验均采用小尺寸拉伸试样。为了消除焊缝形貌对接头性能的影响,所有试样均去除焊缝余高后进行拉伸测试。其中,受测试设备限制,无法测试 3 mm 厚度的高温拉伸试样,所以在焊接试样上切取两个相同尺寸试样后,铣去焊缝下部以获取 2.2 mm 厚的接头上部试样,铣去焊缝上部以获取 1.6 mm 厚的接头下部试样[图 2(b)],测试温度为 1500  $^\circ\text{C}$ 。拉伸后用扫描电子显微镜对断口进行观察分析。

## 3 试验结果显示与分析

### 3.1 平板扫描焊接焊缝规律

在不同激光功率与焊接速度条件下,焊缝熔深的变化规律如图 3 所示。在相同功率下,焊缝深度与焊接速度呈负相关;当焊接速度一定时,焊缝熔深与焊接功率呈正相关。

当功率为 1.5 kW,焊接速度为 2 m/min 时,焊缝形貌为宽而浅的弧形[图 4(a)],焊缝表面熔宽大于焊缝熔深,呈现典型的热导焊缝形貌。当功率为 2 kW,焊接速度为 3 m/min 时,焊缝形貌如图 4(b) 所示,焊

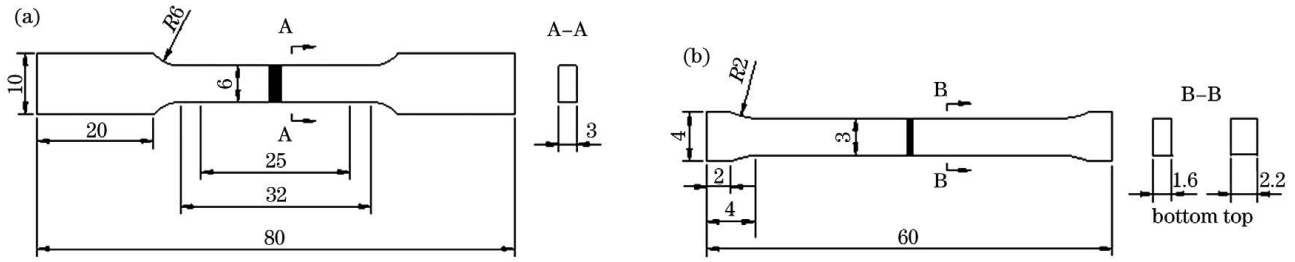


图 2 拉伸试样示意图。(a)室温拉伸试样;(b)1500 °C 高温拉伸试样

Fig. 2 Schematics of tensile specimens. (a) Tensile specimen at room temperature; (b) tensile specimen at 1500 °C high temperature

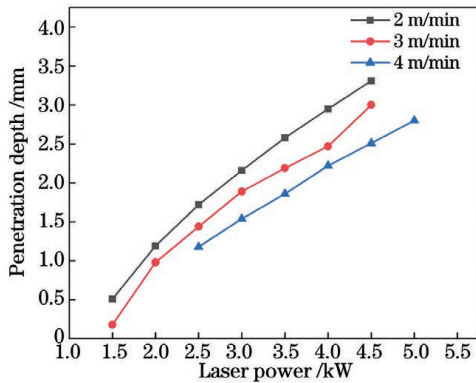


图 3 不同焊接速度下熔深随激光功率的变化

Fig. 3 Penetration depth versus laser power at different welding speeds

缝深度明显大于焊缝表面熔宽,焊缝整体形貌为锥

形,此时的焊缝形貌呈现出深熔焊接特征。当激光功率为 2.5 kW,焊接速度为 2 m/min 时,焊缝整体形貌亦为锥形,焊缝熔深和熔宽同时增加,且焊缝熔深大于焊缝表面熔宽,焊缝形貌呈现出更加明显的深熔焊接特征。如图 3 所示,焊缝熔深随激光功率的变化曲线在 1.5~2.0 kW 范围内的斜率明显大于深熔焊接后的熔深变化斜率,熔深的变化更显著,说明焊接模式在此功率范围内发生了变化。当激光功率为 4.5 kW,焊接速度为 3 m/min 时,焊缝形貌如图 4(d)所示,焊缝深宽比大,焊缝呈激光深熔焊接典型的“钉头”形。热导焊接模式下的焊缝余高较小 [图 4(a)],而较高功率下的深熔焊接焊缝余高较大 [图 4(d)],这与两种焊接模式下的熔池体积及流动特性有关。

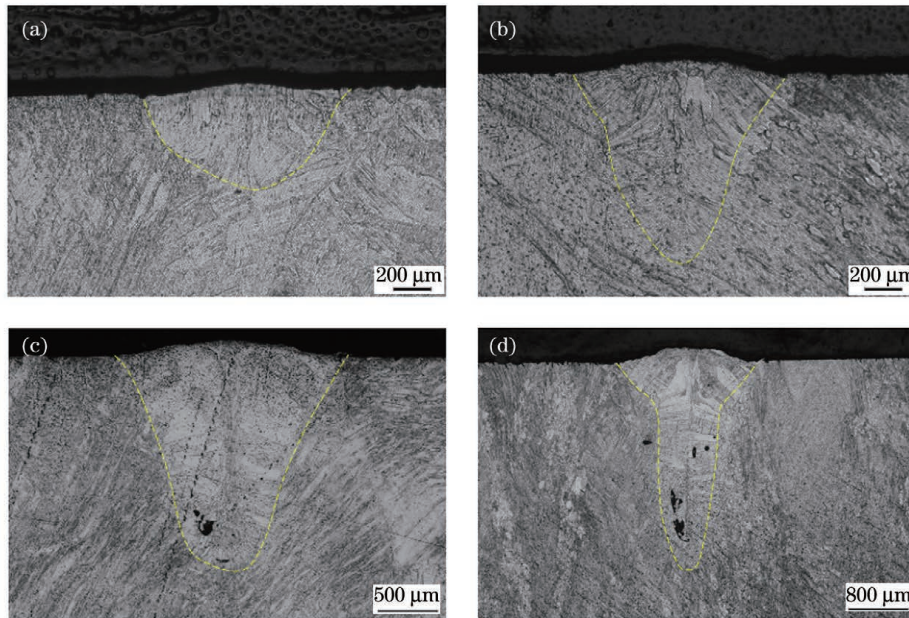


图 4 不同焊接工艺参数下的焊缝形貌图。(a) $P=1.5$  kW,  $v=2$  m/min; (b) $P=2.0$  kW,  $v=3$  m/min; (c) $P=2.5$  kW,  $v=2$  m/min; (d) $P=4.5$  kW,  $v=3$  m/min

Fig. 4 Weld morphologies at different welding parameters. (a)  $P=1.5$  kW,  $v=2$  m/min; (b)  $P=2.0$  kW,  $v=3$  m/min; (c)  $P=2.5$  kW,  $v=2$  m/min; (d)  $P=4.5$  kW,  $v=3$  m/min

### 3.2 对接焊试验结果分析

#### 3.2.1 试样的宏观形貌分析

根据图 3 试验结果可知,当激光功率  $P=4$  kW,焊接速度  $v=2$  m/min,离焦量  $f=0$  mm 时,熔深为

3.0 mm,故采用此参数进行 3 mm 厚的 Ta-10W 对接焊试验。

Ta-10W 对接接头的表面形貌如图 5 所示,焊缝完全熔透,焊缝正面保护及成形良好,焊缝表面为亮白



色,无明显氧化痕迹;接头背部表面光滑,存在轻微凸起,无凹陷缺陷;焊缝表面鱼鳞纹明显,与铝合金和高温合金焊缝表面相比,鱼鳞纹呈圆弧形,且圆弧曲率更小[图 5(c)],这与焊缝熔池长度较短[图 6(d)、(e)]及母材高熔点的物性相关。由高速摄像[图 6(a)~(e)]可以看出,飞溅物脱离熔池,说明焊接过程中飞溅严重,但焊缝

及板材表面附着的飞溅物极少。焊后收集飞溅颗粒进行观测,如图 6(f)所示,尺寸较大的飞溅颗粒在脱离保护气氛后会发生氧化,表面变为蓝色等氧化颜色;而尺寸较小的少量飞溅颗粒表面则保持光亮的颜色,飞溅物多为球状颗粒。这是由于 Ta-10W 的熔点较高,飞溅物落在焊缝及母材表面时就已经凝固。

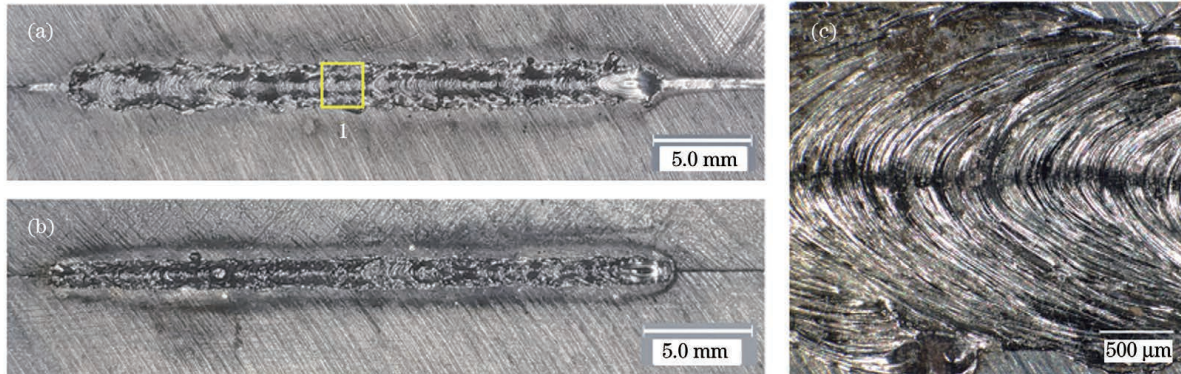


图 5 Ta-10W 对接焊缝的表面宏观形貌。(a)正面;(b)背面;(c)图 5(a)中 1 处的放大图(放大倍率为 100)

Fig. 5 Surface macroscopic morphologies of Ta-10W butt weld. (a) Front side; (b) back side; (c) enlarged view of point 1 in Fig. 5 (a) (magnification of 100)

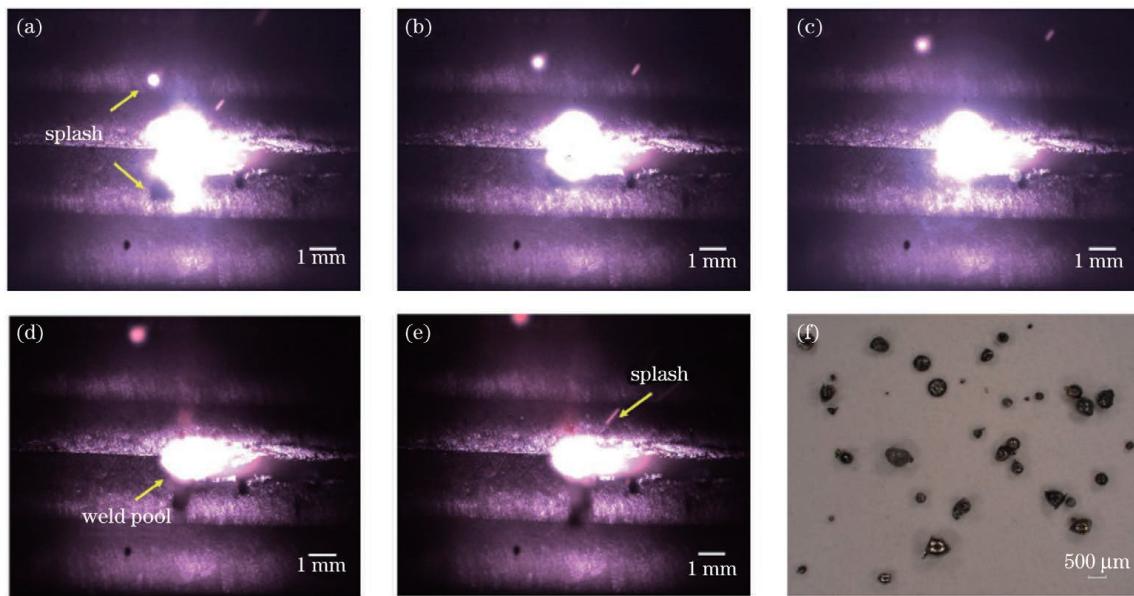


图 6 飞溅脱离熔池的行为与飞溅颗粒的宏观形貌。(a)0 ms;(b)1 ms;(c)2 ms;(d)3 ms;(e)4 ms;(f)飞溅颗粒(放大倍率为 30)

Fig. 6 Behaviors of splash escaping from molten pool and macroscopic morphology of splashing particles. (a) 0 ms; (b) 1 ms; (c) 2 ms; (d) 3 ms; (e) 4 ms; (f) splashing particles (magnification of 30)

### 3.2.2 对接焊缝的显微组织分析

对接接头的宏观形貌及组织如图 7 所示。焊接接头呈典型的钉头形,表面熔宽为 2.26 mm,焊缝钉头部分的下部宽度即腰宽为 1.07 mm[图 7(a)]。其中, BM 为母材区, FZ 为焊缝区, 焊缝组织主要为柱状晶。对比焊缝中心不同位置的组织发现, 焊缝中心不同位置处晶粒的形态与尺寸有较大区别。其中, 在焊缝中心靠上的位置, 形成的是垂直于板厚方向的细长晶粒, 长度可达几百微米, 直径仅几十微米[图 7(b)]; 而在焊缝中心中部与下部位置, 形成的则是细等轴晶粒, 晶粒直径仅几十微米[图 7(c)]。

从焊缝熔合线的局部放大图[图 7(d)、(e)]中可发现, 与铝、钢及高温合金等材料的激光深熔焊缝相比, Ta-10W 焊缝的熔合线不明显, 只能通过熔合线附近的细小重结晶晶粒及柱状晶生长方向来判断熔合线的位置[如图 7(a)、(d)、(e)虚线处]。原因主要为 Ta-10W 合金中的 Ta 的含量(质量分数)高达 90%, 且在焊接时熔池内熔体的黏度较小、流动性强<sup>[9]</sup>。

### 3.2.3 对接焊缝性能测试及断口形貌分析

对 Ta-10W 对接接头的显微硬度进行测试, 试验力为 1.96 N, 载荷时间为 15 s, 测试位置为板厚中央处, 测试点间距为 150 μm。测试结果如图 8 所示, 可



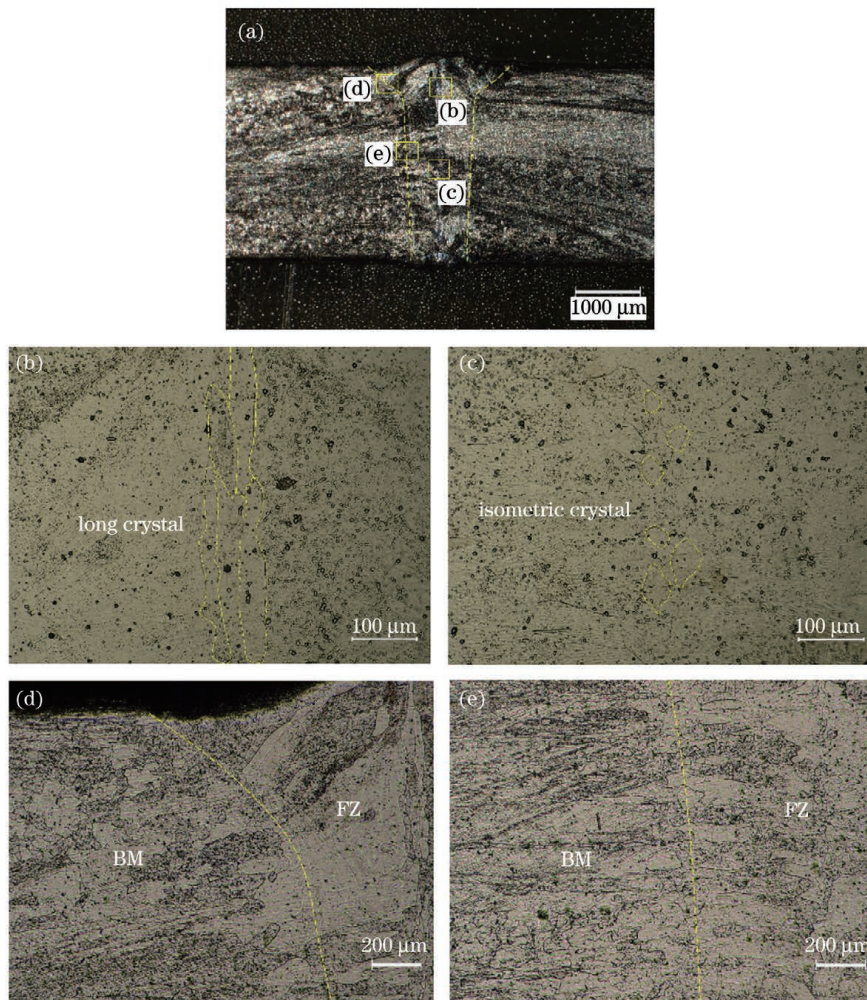


图 7 接头微观组织。(a)宏观形貌；(b)焊缝中心上部；(c)焊缝中心下部；(d)熔合线上部；(e)熔合线中部  
 Fig. 7 Microstructure of joint. (a) Macroscopic morphology; (b) upper part of weld center area; (c) lower part of weld center area; (d) upper part of fusion line; (e) middle part of fusion line

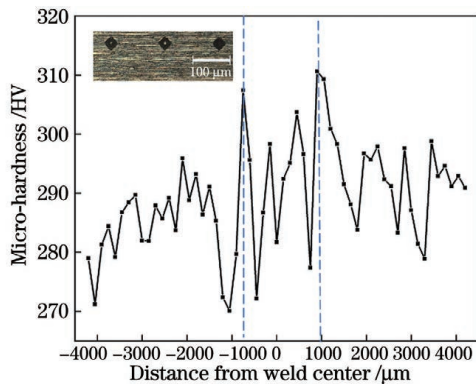


图 8 对接接头的显微硬度分布  
 Fig. 8 Micro-hardness distribution of butt joint

见焊缝区显微硬度波动较大。其中,焊缝最高硬度可达 311 HV,最小硬度为 271 HV,平均硬度为 294 HV,母材显微硬度值基本在 280 HV 左右。焊缝熔合线附近的显微硬度波动最为剧烈,这与熔合线附近区域的受热条件及晶粒尺寸细化有关。

焊接接头的力学性能如图 9 所示,其中右上为三种试样拉断后的照片。焊接接头的拉伸测试结果显

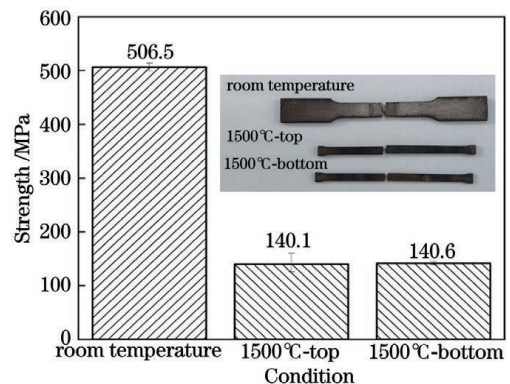


图 9 接头的抗拉强度  
 Fig. 9 Tensile strength of joint

示,接头的室温平均抗拉强度为 506.5 MPa,为母材室温抗拉强度(550 MPa)的 92.1%;在 1500 °C 高温测试时,焊缝上部试样的平均抗拉强度为 140.1 MPa,焊缝下部试样的平均抗拉强度为 141.6 MPa,试样均断裂在母材,说明 Ta-10W 的激光焊接接头具有良好的室温与高温力学性能。

室温接头的断口形貌如图 10 所示。断裂发生在



焊缝位置,呈现沿晶断裂与解理断裂的混合断裂特征。断口上下边缘部分区域具有明显的剪切唇[图 10(a)],表面光滑、颜色较暗,断口剪切唇与拉伸方向大致成 45°,高倍放大下这部分材料发生明显的塑性变形[图 10(b)]。断口左右两侧粗糙不平[图 10(c)],在高倍放大下可以看到典型的冰糖状花

样[图 10(d)],说明发生了沿晶断裂。另外,断口中部存在典型的解理刻面、解理台阶和几处裂纹[图 10(e)],高倍放大下可看到典型的河流花样[图 10(f)],说明该位置发生了解理断裂。

焊缝高温断口形貌如图 11 和图 12 所示。其中,焊缝上部试样的高温断口的形貌显示,断口中部区域

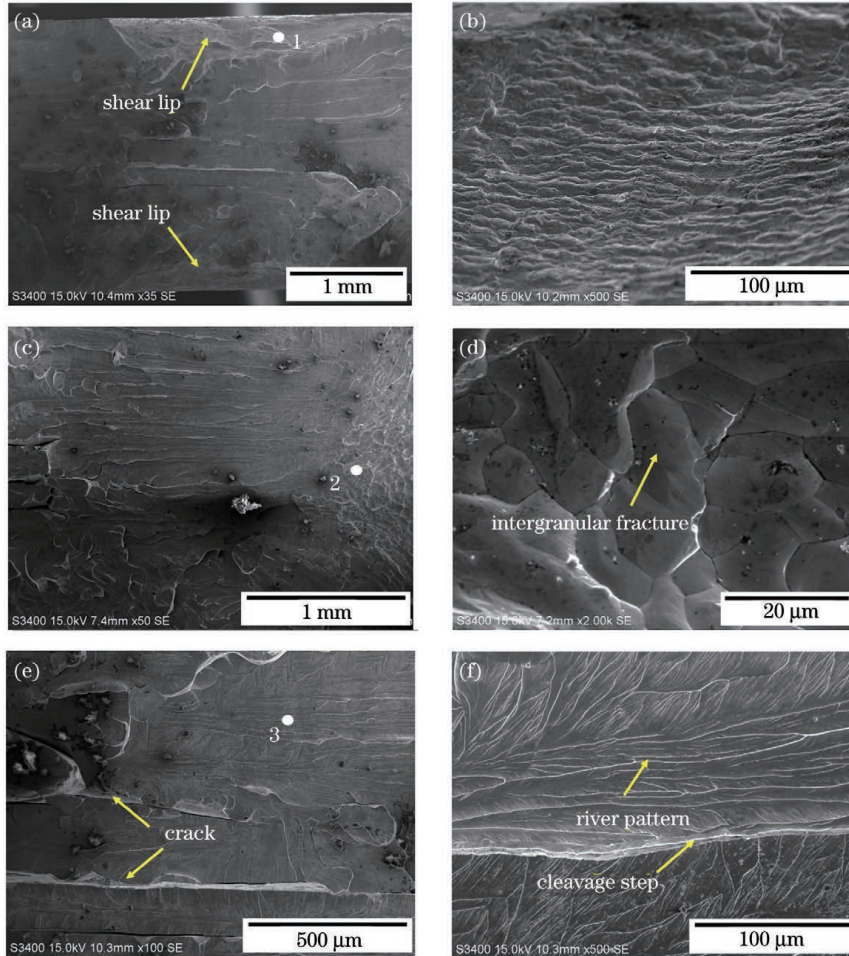


图 10 拉伸试样的室温断口。(a)断口宏观形貌(35×);(b)图 10(a)中 1 处的放大图(500×);(c)断口右侧形貌(50×);(d)图 10(c)中 2 处的放大图(2000×);(e)断口中部形貌(100×);(f)图 10(e)中 3 处的放大图(500×)

Fig. 10 Fracture of tensile specimen at room temperature. (a) Macroscopic morphology of fracture (35×); (b) enlarged view of point 1 in Fig.10(a) (500×); (c) right morphology of fracture (50×); (d) enlarged view of point 2 in Fig.10 (c) (2000×); (e) middle morphology of fracture (100×); (f) enlarged view of point 3 in Fig.10 (e) (500×)

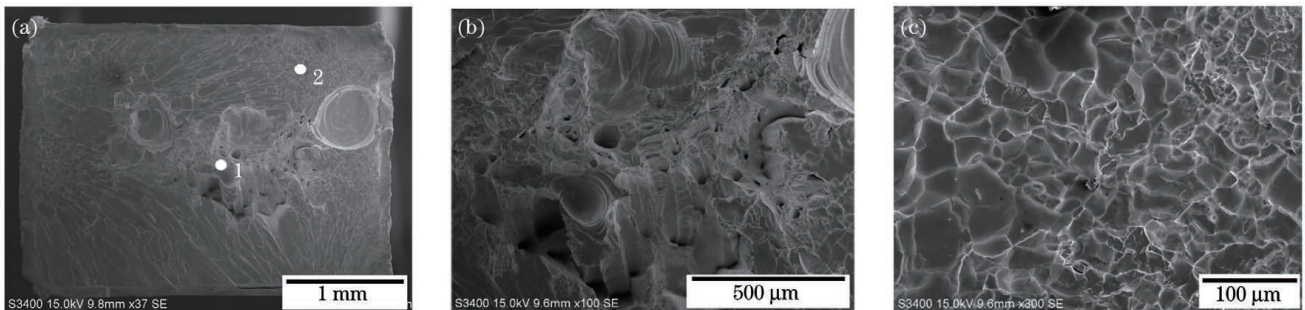


图 11 上部试样的 1500 °C 高温断口。(a)断口宏观形貌(37×);(b)图 11(a)中 1 处的放大图(100×);(c)图 11(a)中 2 处的放大图(300×)

Fig. 11 Fracture of upper specimen at 1500 °C high temperature. (a) Macroscopic morphology of fracture (37×); (b) enlarged view of point 1 in Fig.11 (a) (100×); (c) enlarged view of point 2 in Fig.11 (a) (300×)

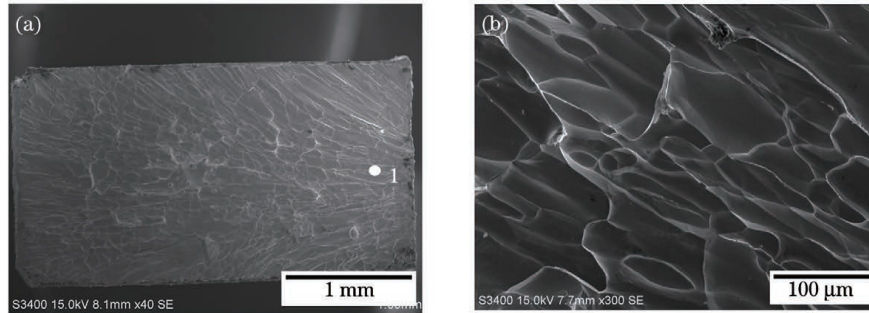


图 12 下部试样的 1500 °C 高温断口。(a)断口宏观形貌(40×);(b)图 12(a)中 1 处的放大图(300×)

Fig. 12 Fracture of lower specimen at 1500 °C high temperature. (a) Macroscopic morphology of fracture (40×); (b) enlarged view of point 1 in Fig. 12 (a) (300×)

产生许多大而深的塑性韧窝[图 11(a)],并伴随着明显的滑移现象,晶粒间无明显界面[图 11(b)];母材中的微小气孔在外力作用下发生变形,变为不规则的椭圆状;断面周围的放射状区域在高倍放大下主要为冰糖状的沿晶断裂形貌,存在部分穿晶断裂特征,晶界干净、光滑,无析出相分布[图 11(c)]。

焊缝下部试样的高温断口形貌如图 12 所示。与上部试样断口相比,断口表面无气孔缺陷,整体呈现放射状花样[图 12(a)]。这是由于裂纹源位于试样表面,裂纹在拉力的作用下发生扩展,最后导致该断口形貌。高倍放大下断口主要呈冰糖状花样的沿晶断裂形貌,晶粒在高温与外力作用下被拉长,发生明显变形[图 12(b)]。

## 4 结 论

获取了 Ta-10W 材料的光纤激光深熔焊接阈值曲线。由于材料的高熔点物性特点,深熔焊接时熔池较小,焊缝呈钉头形貌。当聚焦光斑直径为 0.3 mm,焊接速度为 2~3 m/min 时,Ta-10W 的多模光纤激光深熔焊接的临界功率范围为 1.5~2.0 kW。当激光功率为 4 kW,速度为 2 m/min 时,3 mm 厚的 Ta-10W 对接接头成形良好。沿焊缝深度方向,焊缝中心位置的晶粒形态有较大差异,接头上部分为细长晶粒,中下部为等轴晶粒。焊缝显微硬度略高于母材,焊缝的室温拉伸强度为 506.5 MPa,为母材拉伸强度的 92.1%,断口呈混合断裂特征;1500 °C 高温拉伸强度约为 140.9 MPa,为母材室温强度的 25.6%,断口呈现典型的沿晶断裂特征。研究结果表明,在大气环境下,采用光纤激光可以实现 Ta-10W 这种难熔合金的有效连接。

## 参 考 文 献

[1] 殷为宏, 汤慧萍. 难熔金属材料深加工技术[M]. 北京: 化学工业出版社, 2015.  
Yin W H, Tang H P. Downstream processing technology for refractory metals[M]. Beijing: Chemical Industry Press, 2015.

[2] 郑欣, 白润, 王东辉, 等. 航天航空用难熔金属材料的研究进展[J]. 稀有金属材料与工程, 2011, 40(10): 1871-1875.  
Zheng X, Bai R, Wang D H, et al. Research development of

refractory metal materials used in the field of aerospace[J]. Rare Metal Materials and Engineering, 2011, 40(10): 1871-1875.

[3] Shabalin I L. Ultra-high temperature materials[M]//A comprehensive guide and reference book. Dordrecht: Springer, 2014.

[4] Ellis E A I, Sprayberry M A, Ledford C, et al. Processing of tungsten through electron beam melting[J]. Journal of Nuclear Materials, 2021, 555: 153041.

[5] Senthilnathan N, Annamalai A R, Venkatachalam G. Sintering of tungsten and tungsten heavy alloys of W-Ni-Fe and W-Ni-Cu: a review[J]. Transactions of the Indian Institute of Metals, 2017, 70(5): 1161-1176.

[6] Luo S B, Xu D Q, Song J W, et al. A review of regenerative cooling technologies for scramjets [J]. Applied Thermal Engineering, 2021, 190(2): 116754.

[7] 丁旭. 高钨含量钼合金氩弧焊接工艺研究[J]. 西安文理学院学报(自然科学版), 2010, 13(4): 61-63.  
Ding X. Experimental research of argon-arc welding of Ta-12W alloy[J]. Journal of Xi'an University of Arts & Science (Natural Science Edition), 2010, 13(4): 61-63.

[8] Tao F, Li D, Jia S D, et al. Effect of solution treatment on the microstructure of dissimilar welding joints of Ta-10W and GH3128[J]. Materials Research Express, 2021, 8(6): 066527.

[9] Chen G Q, Yin Q X, Shu X, et al. Microstructure and properties of electron beam welded joints of tantalum and tungsten[J]. Welding in the World, 2018, 62(4): 775-782.

[10] 陈国庆, 张秉刚, 吴双辉, 等. TC4/Ta-W 合金异种金属电子束焊接[J]. 焊接学报, 2011, 32(8): 21-24, 114.  
Chen G Q, Zhang B G, Wu S H, et al. Electron beam welding of TC4/Ta-W alloys dissimilar metal[J]. Transactions of the China Welding Institution, 2011, 32(8): 21-24, 114.

[11] Luo G Q, Zhang J, Li M J, et al. Interfacial microstructure and mechanical strength of 93W/Ta diffusion-bonded joints with Ni interlayer [J]. Metallurgical and Materials Transactions A, 2013, 44(2): 602-605.

[12] 杨永强, 吴世彪, 张越, 等. 光纤激光器在金属增材制造中的应用进展及展望[J]. 中国激光, 2020, 47(5): 0500012.  
Yang Y Q, Wu S B, Zhang Y, et al. Application progress and prospect of fiber laser in metal additive manufacturing [J]. Chinese Journal of Lasers, 2020, 47(5): 0500012.

[13] 顾冬冬, 张红梅, 陈洪宇, 等. 航空航天高性能金属材料构件激光增材制造[J]. 中国激光, 2020, 47(5): 0500002.  
Gu D D, Zhang H M, Chen H Y, et al. Laser additive manufacturing of high-performance metallic aerospace components[J]. Chinese Journal of Lasers, 2020, 47(5): 0500002.

[14] 和岳, 武强, 邹江林, 等. 薄板铝合金光纤激光压焊坡口内材料的熔化行为[J]. 中国激光, 2017, 44(6): 0602008.  
He Y, Wu Q, Zou J L, et al. Melting behavior of materials in grooves during fiber laser pressure welding of thin-sheet aluminum alloy[J]. Chinese Journal of Lasers, 2017, 44(6): 0602008.

[15] Sun J H, Ren W J, Nie P L, et al. Study on the weldability,



- microstructure and mechanical properties of thick Inconel 617 plate using narrow gap laser welding method[J]. *Materials & Design*, 2019, 175: 107823.
- [16] 曹政, 姜仁杰, 杜伟哲, 等. 薄壁结构激光焊接随焊高频冲击变形控制[J]. *中国激光*, 2020, 47(9): 0902003.
- Cao Z, Jiang R J, Du W Z, et al. Distortion control by in-site high frequency peening in laser welding of thin-walled structures[J]. *Chinese Journal of Lasers*, 2020, 47(9): 0902003.
- [17] 江伟, 谢小柱, 魏昕, 等. 脉冲光纤激光控制断裂切割超薄钛酸锶陶瓷基片[J]. *中国激光*, 2016, 43(5): 0503008.
- Jiang W, Xie X Z, Wei X, et al. Pulse fiber laser controlled fracture cutting of ultrathin strontium titanate ceramic substrate[J]. *Chinese Journal of Lasers*, 2016, 43(5): 0503008.
- [18] Zou J L, Yang W X, Wu S K, et al. Effect of plume on weld penetration during high-power fiber laser welding[J]. *Journal of Laser Applications*, 2016, 28(2): 022003.
- [19] Zhang G L, Zhu B Q, Zou J L, et al. Correlation between the spatters and evaporation vapor on the front keyhole wall during fiber laser keyhole welding[J]. *Journal of Materials Research and Technology*, 2020, 9(6): 15143-15152.

## Process Research on Fiber Laser Welding of Ta-10W Refractory Alloy

Du Xin, Qi Baixin, Zhao Zhenjia, Zhang Tong, Wu Qiang<sup>\*</sup>, Zou Jianglin, Xiao Rongshi

*High-Power and Ultrafast Laser Manufacturing Lab, Faculty of Materials and Manufacturing, Beijing University of Technology, Beijing 100124, China*

### Abstract

**Objective** As a refractory alloy, Ta-10W has the advantages of high melting point, good high temperature strength, and low linear expansion coefficient. It has a good application prospect in the manufacturing of components under high thermal service conditions in the aerospace field. However, the traditional welding methods such as electron beam welding and argon arc welding have high costs and large heat input, so it is difficult to obtain high-quality Ta-10W joints with them. In contrast, this material has a high absorptivity and the fiber laser can be implemented in the atmospheric environment, but the relevant work has not been reported. In this paper, the effect of fiber laser welding parameters on weld morphology is studied, the butt-welding process test is carried out, and the structure and properties of the joint are analyzed.

**Methods** The welding equipment adopts a YLS-6000 fiber laser with focusing parameter of  $K_f = 8 \text{ mm} \cdot \text{mrad}$ , wavelength of 1060–1070 nm, transmission fiber core diameter of 200  $\mu\text{m}$ , collimating lens focal length of 200 mm, focusing lens focal length of 300 mm, and focusing spot diameter of 0.3 mm. The Ta-10W refractory alloy sheet is selected as the test material. The size of the plate scanning sample is 50 mm $\times$ 20 mm $\times$ 4 mm, and the thickness of the butt-welding sample is 3 mm. In the welding process, argon gas is used as the shielding gas, and the back protecting tool and the protective nozzle are used as the two-way protection. When the plate is scanned, the welding speed and laser power are also changed. The welding parameter is 4 kW, the welding speed is 2 m/min, and the defocusing amount is 0 mm. The changes of the molten pool and the welding spatter are observed with a high-speed video camera. In the high-speed photography, an 808 nm band light source is used as the molten pool illumination light. The microstructure of the welded joint is analyzed, and the micro-hardness of the welded joint is tested. The tensile specimens are prepared to test the mechanical properties at room temperature and high temperature. The microstructure of the joint is observed by the metallographic microscope and the cross section of the tensile fracture specimen is observed by scanning electron microscope (SEM). The micro-hardness of the joint is tested by the hardness tester. The load is 1.96 N and the loading time is 15 s. The tensile testing machine is used to test the tensile properties of welds.

**Results and Discussions** Through the scanning welding of the Ta-10W alloy plate, it is found that the weld depth is negatively correlated with the welding speed under the same power, while the weld penetration depth is positively correlated with the welding power under the same speed. With the increase of welding power, the weld shape gradually changes from a shallow arc shape in heat conduction welding to a nail head shape in deep penetration welding. The penetration depth is about 3 mm when defocusing amount is 0 mm, the welding speed is 2 m/min, and the laser power is 4 kW. There is no obvious oxidation on the surface of the butt joint, which is bright white and well formed. However, due to the high melting point of the base metal, the short weld pool length, the serious spatter phenomenon, and the little spatter on the plate surface, the spatter is solidified before falling back to the base metal. The grain shapes and sizes at different positions in the weld center are quite different. The grains at the upper position are fine equiaxed grains with a diameter of tens of microns, a length of hundreds of microns, and a width of tens of microns perpendicular to the thickness direction of the plate. The micro-hardness test of the joint shows that the micro-hardness of the weld zone fluctuates greatly, and the average hardness is about 294 HV, slightly higher than that of the base metal (280 HV). This is related to the heating condition and the grain size refinement near the fusion line. The results of the tensile test at room temperature and high temperature show that the average tensile strength of the joint is 506.5 MPa, 92.1% of that of the



base metal, the average tensile strength of the upper part of the weld at 1500 °C is 140.1 MPa, and the average tensile strength of the lower part of the weld is 141.6 MPa. The fracture analysis shows that the fracture is an intergranular and cleavage mixed fracture at room temperature, and an inter-granular fracture at high temperature.

**Conclusions** In the focused state, the critical power of deep penetration for multimode fiber laser welding of Ta-10W alloy is in the range of 1.5–2.0 kW when the welding speed is 2–3 m/min. In the deep penetration state, the weld shape is a nail head shape. There is large splash and it is difficult to adhere to the plate surface. When the power is 4 kW and the speed is 2 m/min, the 3 mm thick Ta-10W butt joint is well formed. Along the weld depth direction, there is a large gap in the grain morphology at the weld center, the upper part is slender grains, and the middle and lower parts are equiaxed grains. The micro-hardness of the butt joint is slightly higher than that of the base metal, and the butt joint has good mechanical properties at room temperature and high temperature. The fracture at room temperature is a mixed fracture, and the high temperature part has an inter-granular fracture.

**Key words** laser technique; Ta-10W; refractory alloy; laser welding; microstructure; mechanical properties